Chemical Science

ROYAL SOCIETY OF CHEMISTRY

EDGE ARTICLE

View Article Online
View Journal | View Issue

Cite this: *Chem. Sci.*, 2025, **16**, 20580

All publication charges for this article have been paid for by the Royal Society of Chemistry

Hydroxyl radical generation from H_2O_2 *via* liquid–liquid contact-electro-catalysis

Haimei Li, [abc] Airong Xie,[a] Chengzi Hong,[a] Zichen Wang,[a] Xu Chu,[d] Zhong Lin Wang,*[e] Yi Liu *[f] and Peng Jiang *[ab]

Contact-electro-catalysis (CEC) has emerged as a promising strategy for reactive oxygen species (ROS) generation, primarily through water oxidation reactions (WOR) and oxygen reduction reactions (ORR), forming the foundation of contact-electro-dynamic therapy (CEDT). However, the high energy barrier of the ORR substantially limits the overall catalytic efficiency. Herein, we propose an alternative hydrogen peroxide (H_2O_2) reduction pathway to replace the ORR pathway, enabling the spontaneous generation of hydroxyl radicals (˙OH) without ultrasound assistance. Perfluorocarbon (PFC) nanoemulsions were prepared to construct a PFC–water liquid–liquid interface. Contact electrification at the PFC–water interface induces an interfacial electron-transfer process, wherein the PFC nanoemulsions act as mediators by capturing electrons from hydroxide ions (OH^-) and subsequently transferring them to H_2O_2, thereby generating ˙OH. Furthermore, ultrasound can enhance ˙OH production by increasing the frequency of liquid–liquid contact and facilitating electron release from negatively charged PFC (PFC*) to H_2O_2. Importantly, we demonstrate that this H_2O_2-based CEC pathway represents a previously unrecognized mechanism underlying CEDT. In tumor microenvironments, where H_2O_2 is overexpressed, this mechanism leads to enhanced ROS production and tumor cell death. This work uncovers a hidden catalytic route within the CEDT framework and provides new insights into the application of CEC for tumor therapy.

Received 3rd August 2025
Accepted 28th September 2025

DOI: 10.1039/d5sc05862g

rsc.li/chemical-science

Introduction

Contact-electro-catalysis (CEC) is a novel catalytic strategy that utilizes electron transfer induced by contact electrification (CE) at solid–liquid and liquid–liquid interfaces to initiate interfacial redox reactions.[1–4] The typical CEC process involves the water oxidation reaction (WOR) and oxygen reduction reaction (ORR), generating reactive oxygen species (ROS) free radicals such as hydroxyl radicals (˙OH) and superoxide anions ($˙O_2^-$).[5,6] Since CE is a universal phenomenon observed in a variety of materials, CEC significantly broadens the scope of candidate catalysts and shows great application potential in the fields of energy conversion, environmental remediation and biomedicine.[7–9]

The initiation of CEC reactions typically requires ultrasound to induce high-frequency interfacial CE. However, in such systems, it is challenging to determine whether the resulting ROS radicals are generated *via* the CEC mechanism or through water sonolysis.[4] Recently, Jiang and Wang *et al.* constructed a solid–liquid interface reaction system using capillaries and successfully initiated the CEC reaction without ultrasound assistance. This work provided definitive evidence that the mechanism of the CEC reaction is CE-induced interfacial electron transfer rather than the traditional water sonolysis mechanism.[10] More recently, they revealed that liquid–liquid CE at the perfluorocarbon (PFC)–water interface can activate CEC, enabling ultrasound-assisted generation of ˙OH, thereby expanding the CEC paradigm beyond solid–liquid systems.[11] The mechanism involves fluorine atoms in PFC capturing electrons from hydroxide ions (OH^-) in the aqueous phase in liquid–liquid CE, resulting in negatively charged PFC (designated as PFC*), while OH^- ions lose electrons, generating ˙OH. Importantly, this mechanism has contributed to the development of contact-electro-dynamic therapy (CEDT) for tumor treatment, in which PFC nanoemulsions produce ROS radicals under ultrasound, inducing immunogenic cell death in tumor cells and subsequently

[a]*Department of Orthopedics Trauma and Microsurgery, Zhongnan Hospital of Wuhan University, School of Pharmaceutical Sciences, Wuhan University, Wuhan 430071, China. E-mail: jiangpeng@whu.edu.cn*

[b]*Key Laboratory of Combinatorial Biosynthesis and Drug Discovery (Ministry of Education), Wuhan University, Wuhan 430072, China*

[c]*College of Biomedical Engineering, South-Central Minzu University, Wuhan 430074, China*

[d]*School of Chemistry & School of Materials Sciences and Engineering, Tiangong University, Tianjin 300387, China*

[e]*Beijing Institute of Nanoenergy and Nanosystems, Chinese Academy of Sciences, Beijing 100083, China. E-mail: zhong.wang@mse.gatech.edu*

[f]*School of Chemistry and Materials Sciences & School of Pharmaceutical Sciences, South-Central Minzu University, Wuhan 430074, China. E-mail: yiliuchem@whu.edu.cn*

activating T cell-mediated antitumor immune responses for tumor ablation.

Since CEC catalysts—typically highly electronegative fluoropolymers such as PTFE and FEP—possess strong electron-accepting capabilities, the WOR step, which involves electron transfer from water to the catalyst, occurs relatively easily. In contrast, the ORR step, requiring electron transfer from the catalyst back to dissolved oxygen, faces a higher energy barrier and generally necessitates an additional energy input, such as ultrasound.[12–14] Our previous studies support this: CE between PTFE and water leads to spontaneous ˙OH generation even in the absence of ultrasound, whereas O_2 requires ultrasound assistance to accept electrons from negatively charged PTFE (PTFE*) to produce $˙O_2^-$.[10] These findings indicate that the ORR step is the rate-limiting step in the CEC process. Therefore, developing more efficient reduction pathways to substitute for the ORR is crucial for enhancing the overall catalytic performance of CEC systems.

Hydrogen peroxide (H_2O_2) is a widely employed oxidant for generating ˙OH, with the Fenton reaction serving as a classic example.[15–17] Moreover, H_2O_2 acts as a key intermediate in intracellular ROS interconversion and is typically overexpressed in tumor tissues, rendering it an important substrate for ROS-mediated cancer therapy.[18–20] Additionally, with standard reduction potentials of +1.78 V for H_2O_2 and +1.23 V for O_2, H_2O_2 exhibits greater oxidizing power and a higher propensity to accept electrons. Based on these properties, we proposed an alternative CEC reduction pathway that employs H_2O_2 as the electron acceptor in place of the ORR pathway, thereby enhancing the overall catalytic efficiency of the CEC system. This strategy may unveil a previously hidden catalytic mechanism in CEDT: the overexpressed H_2O_2 in the tumor microenvironment facilitates excessive ˙OH production *via* the CEC mechanism, ultimately inducing tumor cell death.

In this study, we demonstrate for the first time that PFC–water liquid–liquid CE can spontaneously catalyze H_2O_2 to produce ˙OH without ultrasound. This reaction exhibits a higher efficiency in ˙OH production compared to our previously reported work, where PFC catalyzes water to produce ˙OH under ultrasound.[11] We prepared a nanoemulsion of perfluorotributylamine (PFTBA) stabilized with human serum albumin (HSA) to establish a PFC–water interface and investigate the liquid–liquid interfacial CEC (Scheme 1). Under vortex conditions, electrons are transferred from OH^- to PFC, generating ˙OH and imparting a negative charge to the PFC (PFC*). Subsequently, H_2O_2 accepts electrons from PFC*, resulting in

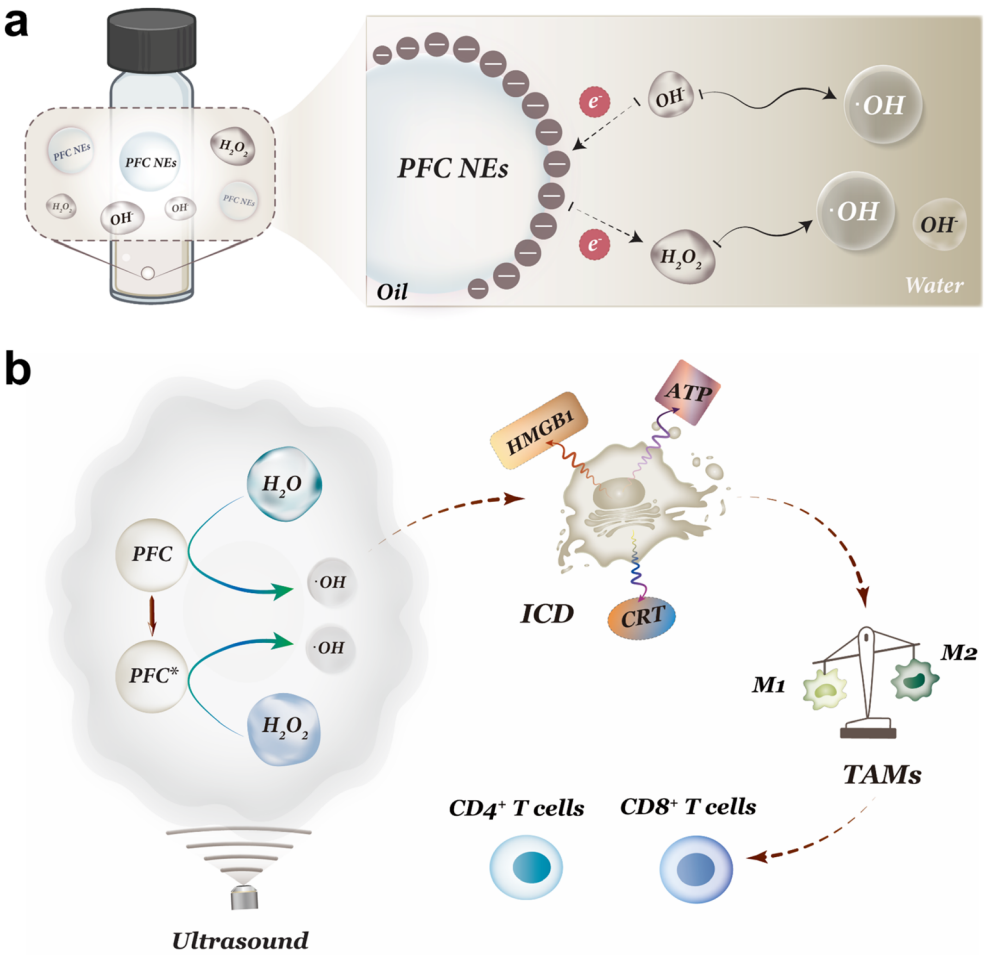

Scheme 1 (a) Schematic illustration of ˙OH generation at the liquid–liquid CE. (b) ˙OH-induced ICD-mediated adaptive immune response.

further ˙OH generation. Moreover, ultrasound can promote the generation of ˙OH, because ultrasound can induce high-frequency liquid–liquid contact and provide energy *via* phonon excitation to promote the release of the electron from PFC back to H_2O_2. In addition, the H_2O_2-based CEC mechanism was demonstrated to be a hidden mechanism in CEDT therapy at the cellular and *in vivo* levels, and the therapeutic effect of CEDT can be enhanced by upregulating intracellular H_2O_2 levels. This work reveals a novel catalytic activity of PFC nanoemulsions and broadens the understanding and application of CEC.

Results and discussion

In this study, we selected PFTBA, a clinically approved PFC,[21–23] to prepare HSA-stabilized PFC nanoemulsions through a classical ultrasound emulsification method (Fig. 1a).[24,25] The prepared PFC nanoemulsions appeared milky white (Fig. 1b), and transmission electron microscopy (TEM) showed a particle size of 89.0 ± 0.9 nm (Fig. S1a and b). At pH 7.0, PFC nanoemulsions carried a negative charge, with a zeta potential of −27.7 mV, which makes it a stable dispersion in aqueous solution.[23] Dynamic light scattering (DLS) analysis determined the hydrodynamic diameter of the PFC nanoemulsions to be 106.6 nm (Fig. S1c). The ultraviolet-visible (UV-vis) absorption spectrum of the PFC nanoemulsions exhibited characteristic peaks corresponding to HSA, confirming the successful modification of the PFC nanoemulsions with HSA (Fig. 1c).

To evaluate the ability of the PFC nanoemulsions to catalyze ˙OH production from H_2O_2, we used 5,5-dimethyl-1-pyrroline *N*-oxide (DMPO) as a spin-trapping agent for detecting ˙OH. As shown in the electron spin resonance (ESR) spectra (Fig. 1d), the PFC–H_2O_2 mixture under vortex treatment exhibited a typical characteristic peak of the DMPO-˙OH spin adduct and a typical signal intensity of 1 : 2 : 2 : 1 was observed, indicating the existence of ˙OH,[11,26] while a negligible DMPO-˙OH signal was observed for the PFC–H_2O reaction under the same conditions. This result confirmed that PFC nanoemulsions can spontaneously catalyze the production of ˙OH from H_2O_2. Notably, in our previously reported work where PFC directly catalyzed the production of ˙OH generation from water, the reaction efficiency was low without ultrasound (as shown in the PFC–H_2O group in Fig. 1d), and ultrasound was required to enhance the production of ˙OH.[11] In comparison, the catalytic reaction in

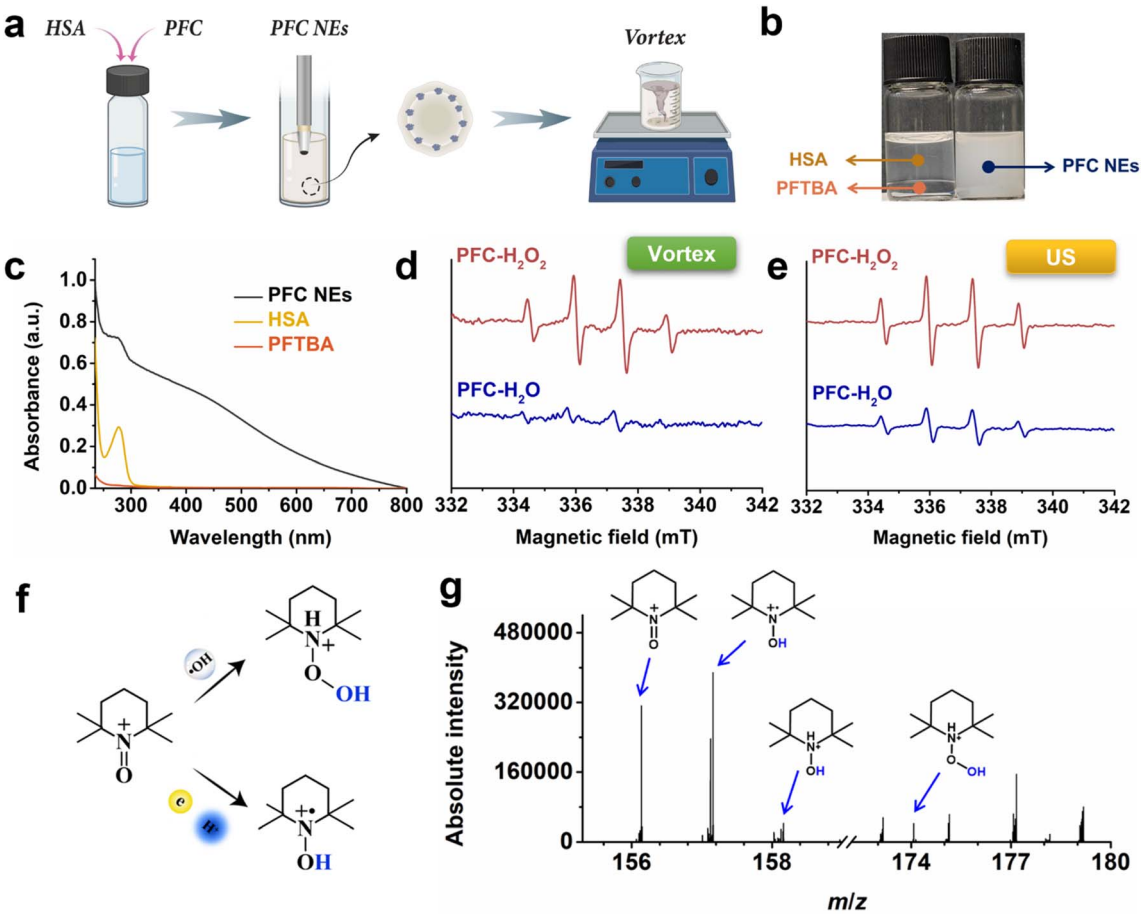

Fig. 1 Characterization of PFC nanoemulsions (NEs) and ˙OH production in the PFC–H_2O_2 catalytic system. (a) Preparation diagram and (b) photograph of PFC nanoemulsions. (c) Absorption spectra of HSA, PFTBA and PFC nanoemulsions. (d and e) DMPO-˙OH ESR spectra of PFC–H_2O_2 and PFC–H_2O solutions treated with vortex (d) and ultrasound (e), respectively. (f) Schematic illustration and (g) mass spectra of radicals and intermediates captured by TEMPO during H_2O_2 catalysis by PFC nanoemulsions.

this study proceeds spontaneously without ultrasound and achieves a significantly higher efficiency in ˙OH generation. Additionally, we also compared the ESR spectra of these two catalytic reactions under the same ultrasonic conditions. As shown in Fig. 1e, the ESR signal of DMPO-˙OH adducts in the PFC–H_2O_2 group with a H_2O_2 concentration of 100 mM is 2.4 times higher than that of the PFC–H_2O group. These results suggest that PFC nanoemulsions can catalyze the production of ˙OH from H_2O_2 more efficiently than water.

Mass spectrometry was subsequently employed to further confirm the ˙OH generation and electron transfer involved in the PFC-catalyzed reaction of H_2O_2 induced by liquid–liquid CE.[27,28] We used radical scavenger 2,2,6,6-tetramethylpiperidine-1-oxyl (TEMPO) to capture reaction intermediates (Fig. 1f).[29,30] The appearance of m/z 157 (TEMPO-H) and m/z 158 (TEMPO-H-H) peaks in the mass spectrum indicated the presence of transferred electrons, while the m/z 174 peak confirmed ˙OH generation through TEMPO-OH (Fig. 1g), consistent with ESR results.

To validate that the formation of ˙OH originates from liquid–liquid CE at the PFC–H_2O interface, we designed and constructed a device to probe PFC–H_2O contact electrification (Fig. 2a and Movie S1). The working principle is analogous to that of a triboelectric nanogenerator (TENG), utilizing the coupling of contact electrification between water droplets and PFC with electrostatic induction to generate an electric signal (Fig. 2a). The results show that when a water droplet first contacts the PFC surface, the droplet–air interface spontaneously carries a small amount of positive charge, resulting in a weak negative current (I_1) (Fig. 2b). However, since liquid–liquid CE occurs between the water droplet and the PFC, some electrons are transferred to the PFC. Therefore, when the droplet detaches from the PFC surface, the positive charge of the water droplet moves away from the PFC, resulting in a charge imbalance and an enhanced current signal (I_2) observed under the action of electrostatic induction. These changes in the current signal confirm that contact electrification occurs between the PFC and the water droplet. After the process reached a stable operating state, the transferred charge per cycle was measured to be approximately 0.003 nC (Fig. 2c).

We propose that PFC nanoemulsions serve as an electron-transfer mediator in the generation of ˙OH. Initially, PFC captures electrons from OH^-, then transfers them to H_2O_2, generating ˙OH, as illustrated in Fig. 3a. To further validate the mechanism of ˙OH generation in the PFC–H_2O_2 catalytic system, DMPO was selected as a spin-trapping agent for

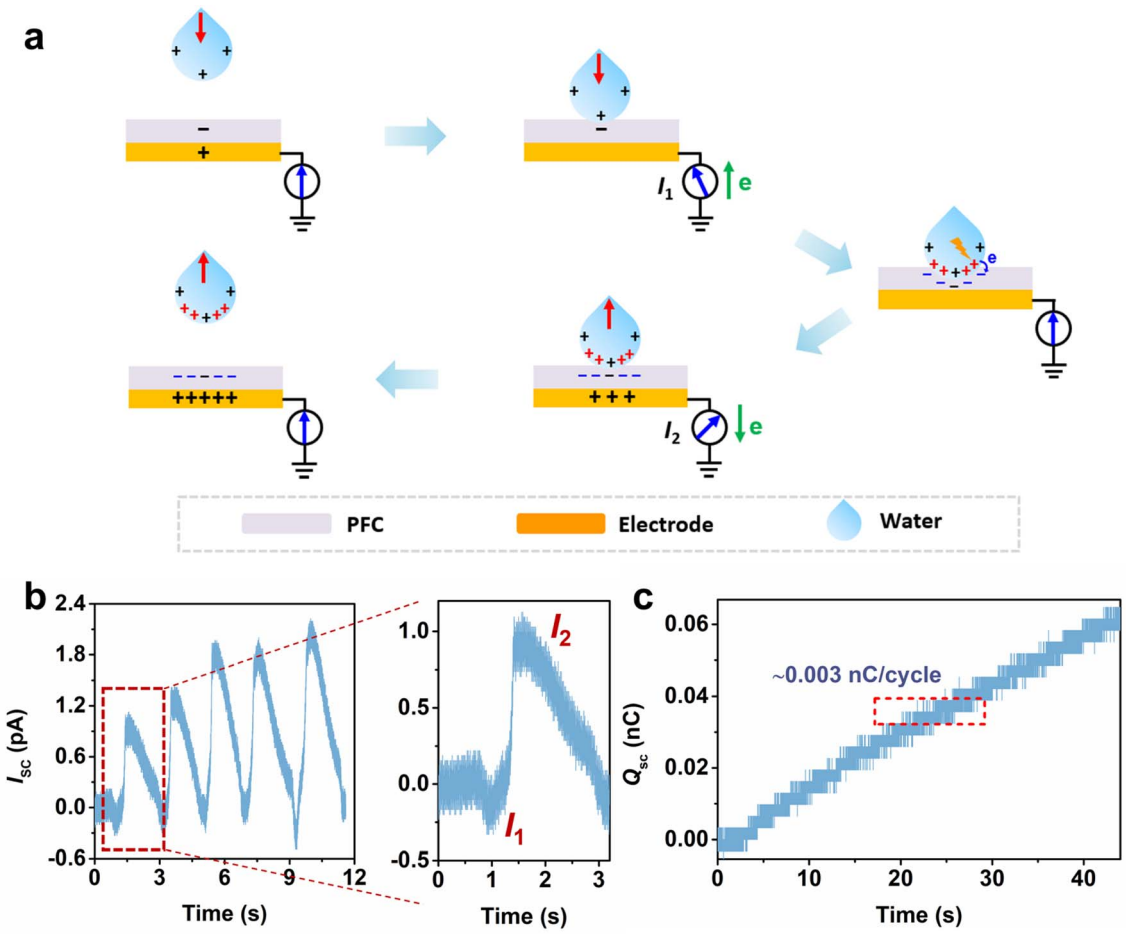

Fig. 2 Mechanism of contact electrification in the PFC–H_2O catalytic system. (a) Schematic illustration of PFC–water liquid–liquid contact electrification. (b) Short-circuit current (I_{SC}) and (c) short-circuit charge transfer (Q_{SC}) in the PFC–H_2O catalytic system.

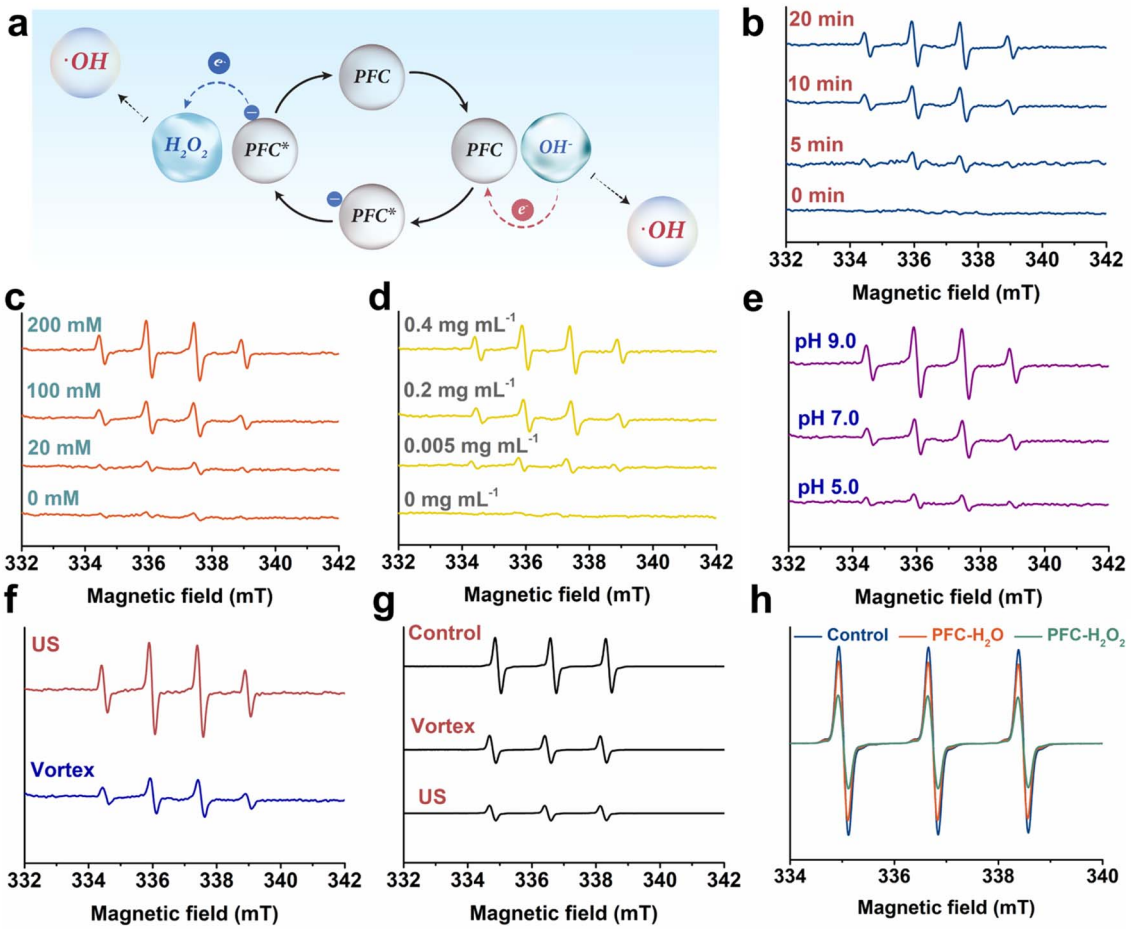

Fig. 3 Mechanism of ˙OH generation in the PFC–H_2O_2 catalytic system. (a) Schematic illustration of ˙OH generation in the PFC–H_2O_2 catalytic system. (b–e) DMPO-˙OH ESR spectra of PFC–H_2O_2 solutions treated with vortex by varying the conditions of vortex time (b), H_2O_2 concentration (c), PFC nanoemulsion concentration (d), and pH (e). (f and g) ESR spectra of DMPO-˙OH (f) and TEMPO (g) of PFC–H_2O_2 solutions treated with vortex and ultrasound, respectively. (h) TEMPO ESR spectra of PFC–H_2O_2 and PFC–H_2O solutions treated with vortex.

detecting ˙OH under various conditions.[26,31] As shown in Fig. 3b, the intensity of the DMPO-˙OH ESR signal increased over time under vortex conditions, indicating the progressive generation of ˙OH. We then varied the H_2O_2 concentration in the PFC–H_2O_2 reaction system while keeping the PFC nanoemulsion concentration constant, and observed that higher H_2O_2 concentrations resulted in increased ˙OH production (Fig. 3c). Similarly, the amount of ˙OH produced increased with higher concentration of PFC nanoemulsions (Fig. 3d). These results demonstrate that ˙OH generation is catalyzed by PFC nanoemulsions in the presence of H_2O_2. Notably, as the pH increased from 5.0 to 9.0, the ESR signal for the DMPO-˙OH adduct significantly enhanced (Fig. 3e). This can be attributed to two factors: first, the increased OH^- concentration raises the PFC-catalyzed conversion of OH^- to ˙OH.[10,11] Second, the electron transfer from OH^- to PFC also increases, allowing H_2O_2 to acquire more electrons from the negatively charged PFC, resulting in more ˙OH production. We further investigated the impact of ultrasound on ˙OH generation. As shown in Fig. 3f, ultrasonication of the PFC–H_2O_2 mixture for 10 min resulted in a notably stronger ESR signal for the DMPO-˙OH adducts compared to vortex treatment alone. This enhancement may be attributed to the higher frequency of liquid–liquid contacts induced by ultrasound, along with phonon excitation to facilitate electron release from the PFC to H_2O_2 in the aqueous solution.[11]

To investigate electron transfer in the PFC–H_2O_2 catalytic system, we used ESR spectra of TEMPO to analyze the electron transfer in the catalytic process. TEMPO is a stable free radical that can react with one electron and one proton to form non-paramagnetic TEMPOH, thereby reducing the ESR signal of TEMPO.[32,33] First, the differences in electron transfer between vortex and ultrasonic conditions were investigated. As shown in Fig. 3g, the TEMPO ESR intensity of PFC–H_2O_2 solutions decreased significantly in both the vortex (vortex group) and ultrasound (US group) treatments compared to the control group, with rapid signal decreases over time (Fig. S2), confirming electron transfer of the PFC–H_2O_2 catalytic system in both the vortex group and US group. Moreover, the greater reduction in ESR signal in the US group relative to the vortex group indicates that ultrasound promotes interfacial electron exchange, enhancing ˙OH generation, consistent with the

conclusions in Fig. 3f. Then, the ESR spectra of TEMPO in the PFC–H_2O and PFC–H_2O_2 groups were also measured to investigate the electron transfer at different stages of the catalytic reaction. As illustrated in Fig. 3h, the TEMPO ESR intensity decreased significantly in both the PFC–H_2O_2 and PFC–H_2O groups with vortex treatment compared to the control group, indicating electron transfer in both groups. Additionally, the decrease in TEMPO's ESR signal was more pronounced in the PFC–H_2O_2 group than in the PFC–H_2O system, confirming electron transfer in the PFC-catalyzed reaction with H_2O_2.

Subsequently, we further investigated the ˙OH generation mechanism using methylene blue (MB), *o*-phenylenediamine (*O*PD), and terephthalic acid (TA) as probes. MB degradation by ˙OH causes a decrease in absorbance at 664 nm.[19,34] OPD oxidation by ˙OH produces 2,3-diaminophenazine (DAP), with a characteristic absorption peak at 415 nm.[35] TA oxidation by ˙OH results in 2-hydroxyterephthalic acid (TAOH), which shows a characteristic fluorescence peak at 425 nm.[36] As shown in Fig. 4a, PFC nanoemulsions were added to a solution containing H_2O_2 and an ˙OH probe, followed by ultrasonication or vortex treatment. Changes in solution color and corresponding absorption or fluorescence spectra were recorded. As shown in Fig. 4b, after 10 minutes of vortexing, the absorbance of MB at 664 nm significantly decreased, with the solution color changing from deep blue to light blue, indicating that ˙OH produced by the PFC–H_2O_2 catalytic system degraded MB (inset in Fig. 4b). The catalytic activity of PFC nanoemulsions did not exhibit any significant change even after storage in an aqueous solution for 30 days, confirming their long-term stability and robustness for catalytic applications (Fig. S3). Then, the effect of vortex duration on ˙OH generation was further verified (Fig. 4c and S4–S5). As vortex time increased from 0 to 20 min, the absorbance at 664 nm gradually decreased, and the MB color lightened (inset in Fig. 4c). Additionally, increasing the concentrations of H_2O_2 and PFC nanoemulsions also elevated ˙OH production (Fig. 4d, e, g, h, and S5b–c).

Under the same conditions, MB degradation was more pronounced with ultrasound than vortex treatment, indicating

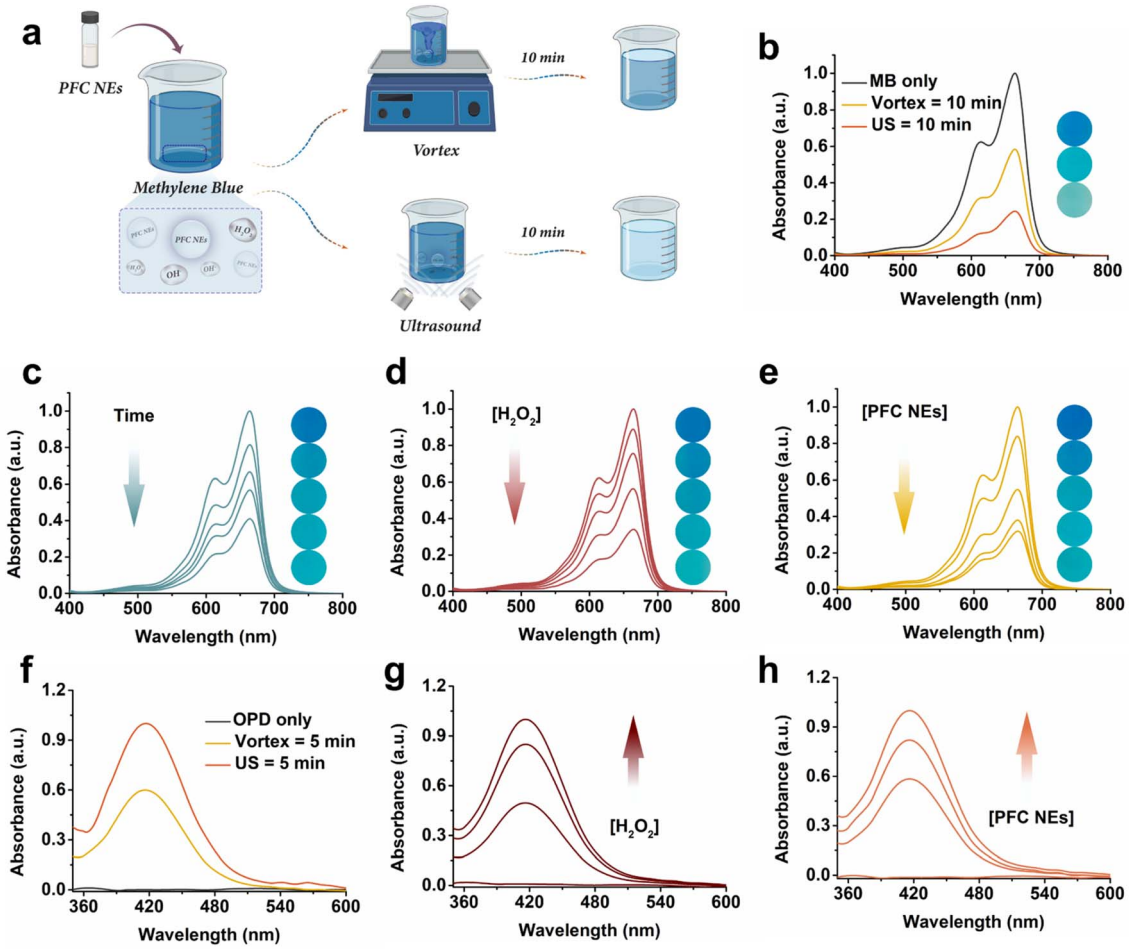

Fig. 4 Investigation of ˙OH generation using various probes. (a) Schematic diagram of the experimental setup and protocol. (b) Absorption spectra and photographs of MB treated with PFC–H_2O_2 mixtures under vortex and ultrasonication, respectively. (c–e) Absorption spectra and photographs of MB treated with PFC–H_2O_2 mixtures under vortex with varying conditions of vortex time (c), H_2O_2 concentration (d), and PFC nanoemulsion concentration (e). (f) Absorption spectra of OPD treated with PFC–H_2O_2 mixtures under vortex and ultrasonication, respectively. (g and h) Absorption spectra of OPD treated with PFC–H_2O_2 mixtures under vortex with varying conditions of H_2O_2 concentration (g) and PFC nanoemulsion concentration (h).

that ultrasonication can enhance the ability of PFC nanoemulsion to catalyze the generation of ˙OH from H_2O_2 (Fig. 4b). The OPD and TA results were consistent with those of MB (Fig. 4f and S4c). In addition, we further verified the effect of ultrasound on H_2O_2 decomposition using the H_2O_2 indicator probe 3,3′,5,5′ -tetramethylbenzidine (TMB) (Fig. S6a). Although ultrasound alone caused approximately 51% H_2O_2 decomposition, this decomposition did not make a dominant contribution to the generation of ˙OH. As shown in Fig. S6b, the resulting ˙OH concentration in H_2O_2 + US group was approximately 28% of that generated by the PFC + H_2O_2 + US group, demonstrating that the contribution of PFC to ˙OH generation is far greater than the ˙OH generated by ultrasound itself decomposing H_2O_2.

These results corroborated ESR data, indicating that liquid–liquid CE in the PFC–H_2O_2 catalytic system under vortex or ultrasound conditions induces interfacial electron transfer, with PFC acting as the electron-transfer mediator to catalyze ˙OH production from H_2O_2.

In addition, density functional theory (DFT) simulations were conducted to evaluate the electron transfer energy band gap (ΔE) between the lowest unoccupied molecular orbital (LUMO) of PFC (PFTBA) and the highest occupied molecular orbital (HOMO) of H_2O_2 in the PFTBA–H_2O_2 system, as well as between the LUMO of PFTBA and the singly occupied molecular orbital (SOMO) of O_2 in the PFTBA–O_2 system. As shown in Fig. 5a, the ΔE for electron transfer at the PFTBA–H_2O_2 interface (0.263 au) is lower than that at the PFTBA–O_2 interface (0.301 au), indicating that electron transfer is more thermodynamically favorable in the presence of H_2O_2. This finding supports the preferential reduction of H_2O_2 by PFC-derived electrons to generate hydroxyl radicals (˙OH), consistent with our previous experimental observations.[38] Based on all the evidence, we propose a mechanism for PFC-catalyzed ˙OH generation from H_2O_2 induced by liquid–liquid CE (Fig. 5b and c). Initially, when PFC nanoemulsions come into contact with an aqueous solution, the overlap of electron clouds between F atoms in PFC and the O atoms in OH^- lowers the transition barrier, enabling electrons to transfer from OH^- to the PFC during the liquid–liquid contact process (Fig. 5b).[1] At this point, OH^- loses an electron and is oxidized to ˙OH (eqn (1) and Fig. 5c left), as reported in our previous work.[11] Simultaneously, the PFC captures the electron and becomes negatively charged (PFC*) (Fig. 5c middle). Subsequently, H_2O_2 dissolved in water collides with PFC* under vortex treatment, captures electrons from PFC* and produces ˙OH again (eqn (2), Fig. 5c right), with PFC* losing its charge and returning to its initial state, completing one catalytic cycle (Fig. 5c left).[1] As vortexing continues, OH^- re-contacts PFC, initiating the next catalytic cycle *via* liquid–liquid CE.[37] When ultrasonication is applied, the cavitation and collapse of bubbles during ultrasonic oscillation induces high-frequency contact between the water solution and PFC nanoemulsion, and provide the energy *via* phonon excitation to assist the release of the electron from PFC* back to H_2O_2, thereby enhancing ˙OH generation.

$$PFC + OH^- \rightarrow PFC^* + {}^{\cdot}OH \quad (1)$$

$$PFC^* + H_2O_2 \rightarrow PFC + OH^- + {}^{\cdot}OH \quad (2)$$

To validate the role of the H_2O_2-based CEC mechanism in CEDT therapy, we investigated the performance of PFC in catalyzing H_2O_2 to generate ˙OH in a biological system.[11] First, glucose oxidase (GOD) was introduced into the cells to elevate the intracellular H_2O_2 concentration,[19] thereby testing whether PFC nanoemulsions can catalyze the conversion of H_2O_2 to ˙OH within the cells. As shown in Fig. 6a, following incubation with GOD (GOD group), the cellular H_2O_2 level increased

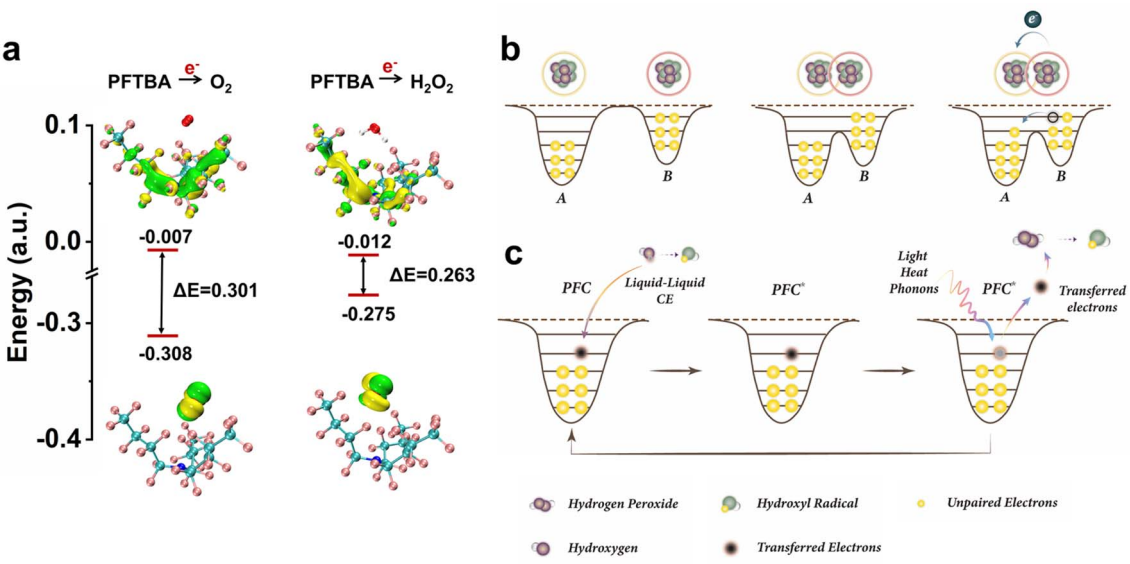

Fig. 5 Schematic illustration of the ˙OH generation mechanism in the PFC–H_2O_2 catalytic system. (a) DFT simulations of the electron transfer energy band gap in different materials. (b) Illustration of electron transfer induced by the electron cloud overlap between two atoms. (c) Description of electron transfer during PFC–water liquid–liquid CE.

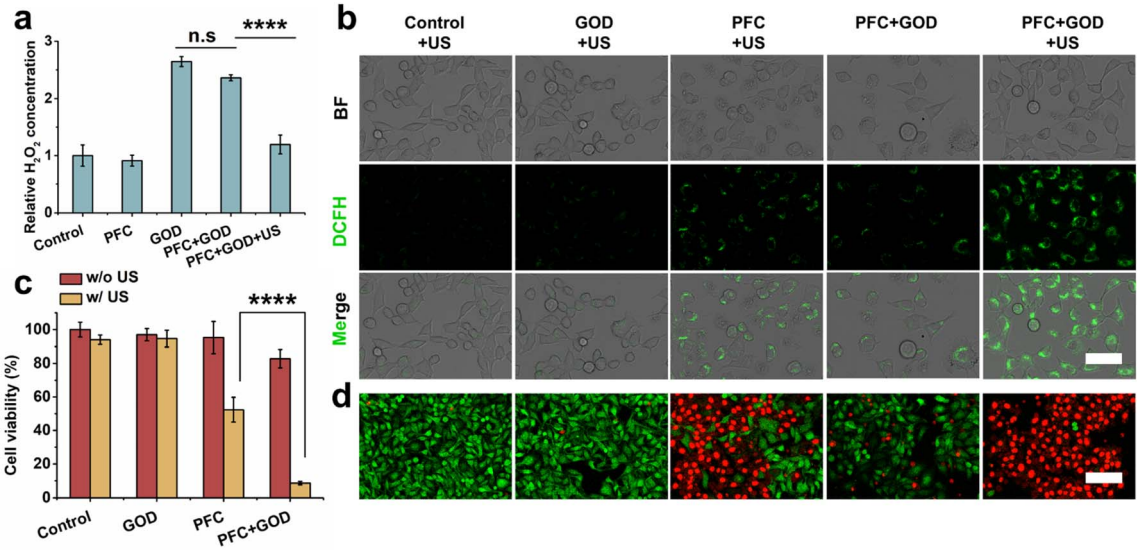

Fig. 6 Validation of PFC-mediated CEDT at the cellular level. (a) Variation of intracellular hydrogen peroxide concentration in 4T1 cells after incubation with different materials. (b) Confocal fluorescence imaging of 4T1 cells releasing ROS under different treatments. DCFH as a probe. Scale bar: 50 μm. (c) Cell viability analysis and (d) confocal fluorescence imaging of 4T1 cells under different treatments. Scale bar: 100 μm. n.s. not significant, *p < 0.1, **p < 0.01, ***p < 0.001, ****p < 0.0001.

significantly. The addition of PFC (PFC + GOD group) resulted in a slight decrease in intracellular H_2O_2 levels. Notably, upon the introduction of ultrasound, the intracellular H_2O_2 content decreased markedly (PFC + GOD + US group). This reduction is attributed to ultrasound-induced high-frequency liquid–liquid CE between water and PFC, which facilitates electron exchange and enables the PFC to catalyze H_2O_2 degradation, thereby generating ˙OH.

Next, DCFH-DA was employed as a probe to visualize changes in intracellular ROS levels *via* confocal laser scanning microscopy (CLSM).[11] As depicted in Fig. 6b, under identical ultrasound conditions, the PFC + US group exhibited significantly enhanced green fluorescence compared to the Control + US group, indicating that PFC under ultrasound can catalyze the generation of ˙OH from both intracellular H_2O_2 and water. Remarkably, the experimental group in which intracellular H_2O_2 levels were increased by GOD (PFC + GOD + US group) demonstrated a further significant enhancement in intracellular ROS levels, as evidenced by the brighter green fluorescence.

The cellular apoptosis induced by CEDT was confirmed using the MTT assay. As shown in Fig. 6c, cell viability remained above 90% in both the PFC group and the Control + US group. However, ˙OH produced by PFC under ultrasound reduced the cell viability to 52.3% (PFC + US group). In the PFC + GOD + US group, the GOD-induced upregulation of H_2O_2 further increased the ˙OH level, resulting in a dramatic decrease in cell viability to 8.6%. Additionally, tumor cell killing by CEDT was further validated *via* live/dead cell staining. As illustrated in Fig. 6d, fluorescence images of dual-stained cells using calcein-AM/PI revealed that cells in the PFC + GOD + US group displayed bright red PI fluorescence (indicating dead cells) with minimal FITC green fluorescence (indicating live cells), confirming that PFC-mediated CEDT exhibits significant antitumor activity by nearly eliminating all tumor cells.

Subsequently, the ROS-mediated cell death mechanism was investigated. Studies have shown that ROS can induce immunogenic cell death (ICD), manifested by the release of ATP and HMGB1 into the extracellular environment and the translocation of calreticulin (CRT) to the cell surface.[39] Accordingly, we measured extracellular ATP levels using an ATP assay kit. As shown in Fig. 7a, no significant differences in ATP secretion were observed among the Control, GOD, and PFC groups. However, upon applying ultrasound in the presence of PFC (PFC + US group), the extracellular ATP level increased relative to the PFC group. Moreover, with the addition of GOD (PFC + GOD + US group), the secreted ATP level further increased to 1.8 times that of the PFC + US group. ELISA results confirmed that the PFC + GOD + US group also induced a higher level of HMGB1 exposure compared to the PFC + US group (Fig. 7b). Furthermore, fluorescence imaging was used to observe the transferred CRT from the endoplasmic reticulum to the cell surface. Compared with other groups, the PFC + GOD + US group showed the strongest green fluorescence, indicating the highest expression of CRT (Fig. 7c). This series of evidence indicates that PFC-mediated ROS generation induces ICD, and the expression of signals such as ATP, HMGB1, and CRT promotes the recruitment of antigen-presenting cells and the activation of the immune response.[39]

The *in vivo* antitumor efficacy of the H_2O_2-based CEC mechanism was validated in tumor-bearing mice. As shown in Fig. 8a, 4T1 solid tumors were subcutaneously inoculated in the right hind leg of the mice, and once the tumor volume reached 100 mm^3, the mice were randomly divided into five groups (n = 5): the Control group, the PFC group, and the PFC + US group, which received injections of PBS (100 μL) and PFC

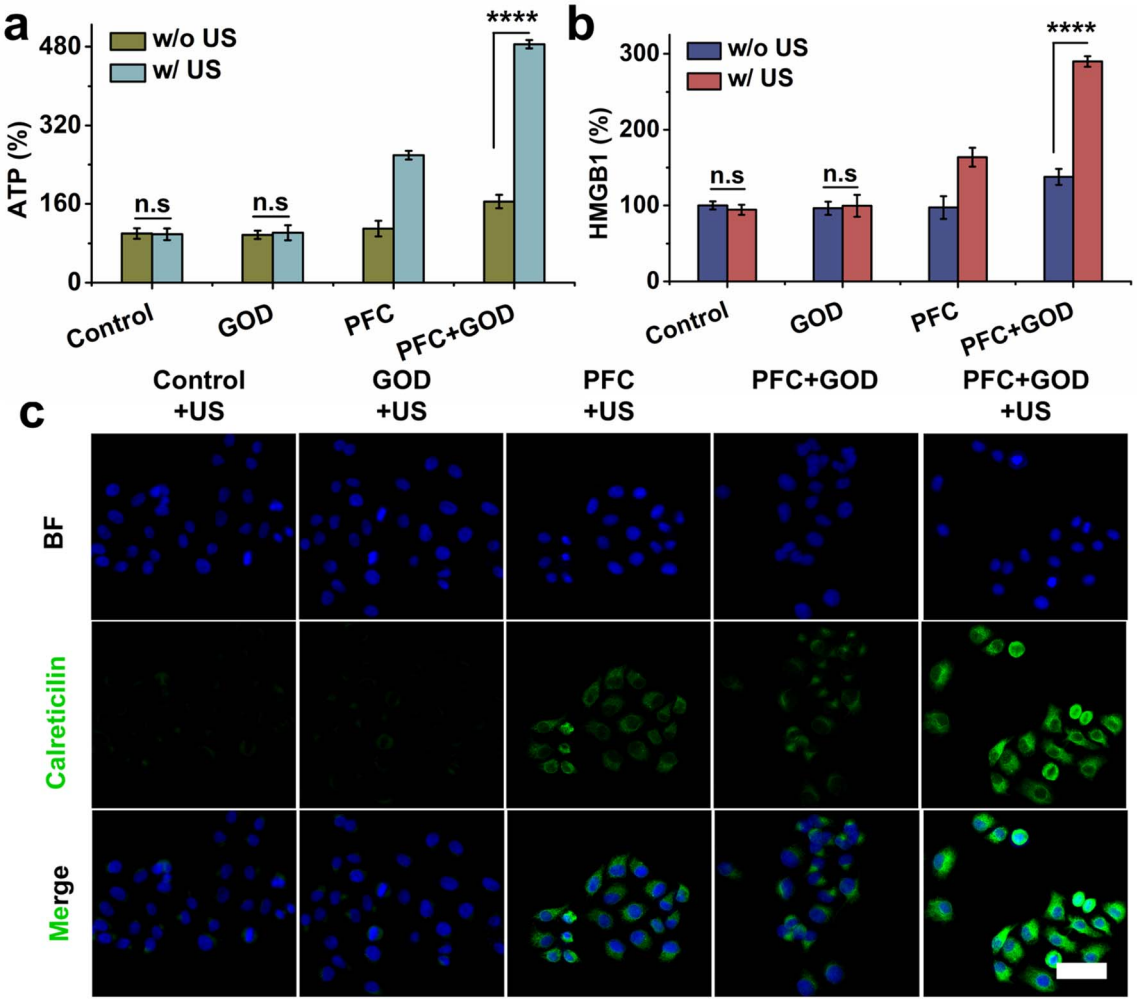

Fig. 7 PFC-mediated mechanisms of immunogenic cell death. Percentage of (a) ATP and (b) HMGB1 secreted into the extracellular environment by 4T1 cells after incubation with different materials with or without ultrasonication. (c) Confocal fluorescence imaging of calreticulin released into the extracellular environment by 4T1 cells under different treatments. Scale bar: 50 μm.

nanoemulsions (2.5 mg kg^{-1}) every two days, respectively; and the PFC + GOD group and the PFC + GOD + US group, which received injections of a mixed solution of PFC nanoemulsions (2.5 mg kg^{-1}) and GOD (75 μg kg^{-1}) at the same interval (100 μL per injection).

In the PFC + US and PFC + GOD + US groups, ultrasound was applied to the tumor sites after injection (3 kHz, 1 W cm^{-2}, 50% duty cycle, 10 min). During the treatment period, physiological data were collected at corresponding time points (Fig. 8b–e). As shown in Fig. 8b, tumors in the Control and PFC groups maintained rapid growth over the 14 days treatment period, with both tumor volume and weight remaining high after 14 days (Fig. 8c and d). However, tumor growth in the PFC + US group was suppressed. To validate the contribution of the H_2O_2-based CEC mechanism, GOD was infused into the tumor sites to elevate intratumoral H_2O_2 levels. Under the same ultrasound conditions, the simultaneous administration of PFC and GOD (PFC + GOD + US group) led to significant tumor growth inhibition, even resulting in the complete eradication of solid tumors. Moreover, no significant differences in body weight were observed among the groups during the treatment period (Fig. 8e), demonstrating the favorable biosafety of this therapy and maintaining the overall health of the mice.

Subsequently, the ROS levels within the tumor tissues were evaluated using dihydroethidium staining. As shown in Fig. 8f, tumor tissues in the PFC + GOD + US group exhibited the brightest red fluorescence, confirming that under ultrasound, tumor cells in this group produced the highest ROS levels, which are responsible for inducing cellular damage. The extent of tumor tissue damage was further verified; as expected, H&E and TUNEL staining results indicated that tumor tissues in the PFC + GOD + US group experienced the most severe damage compared to the other groups, and Ki67 staining further confirmed that tumor cell proliferation was significantly inhibited in this group.[11]

Collectively, these findings confirm that the ROS generation pathway in the CEDT is not solely reliant on the previously reported WOR and ORR CEC mechanisms, but also involves an alternative CEC mechanism based on an H_2O_2 reduction pathway. This represents the hidden mechanism underlying

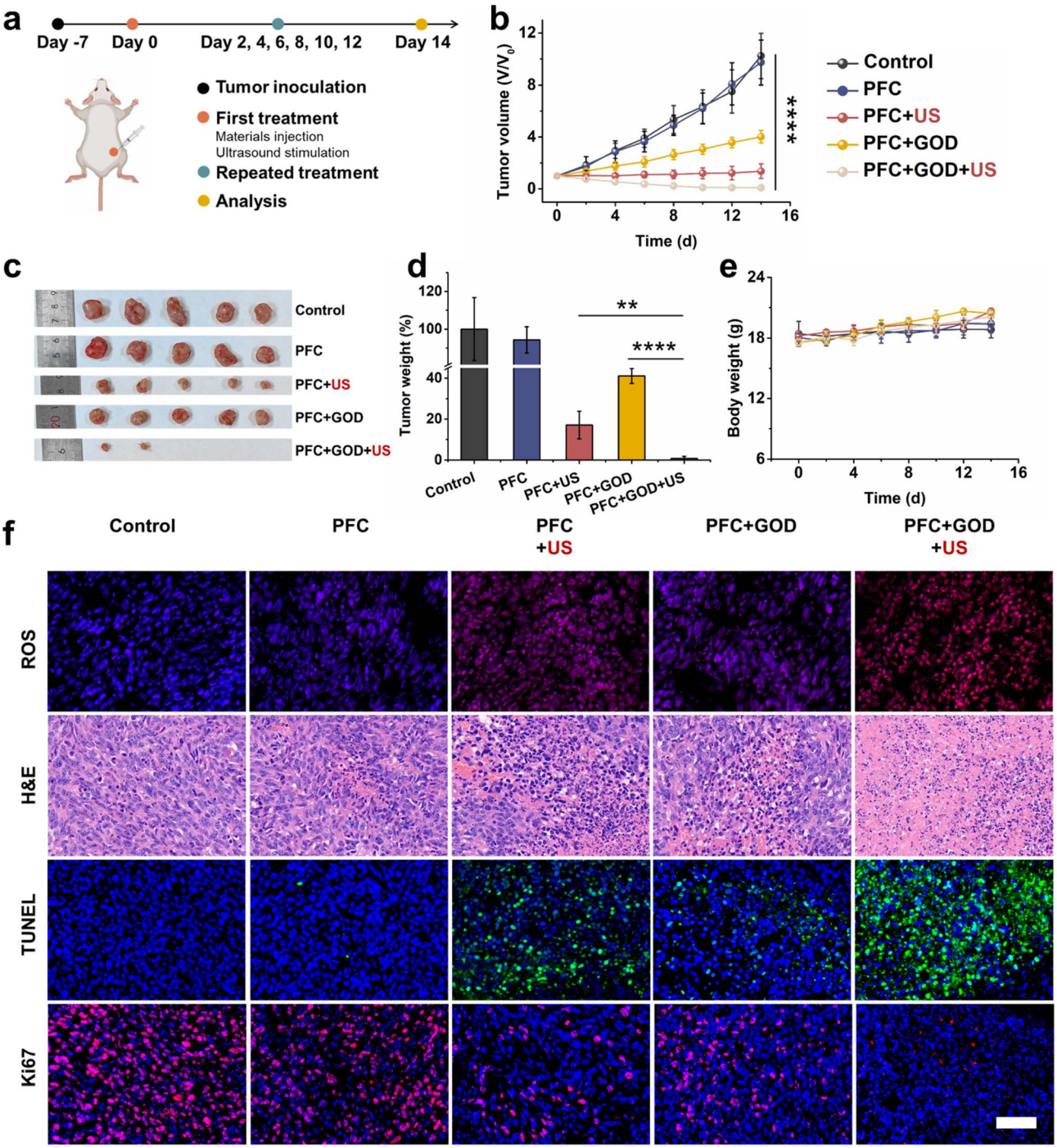

Fig. 8 Validation of PFC-mediated CEDT *in vivo*. (a) Schematic illustration of 4T1 tumor-bearing mice model construction and treatment. (b) Tumor growth curves, (c) photographs of tumors, (d) tumor weight, and (e) body weight of mice under different treatments. (f) Representative microscopic images of ROS, H&E, TUNEL, and Ki67 staining of tumor areas. Scale bar: 100 μm. n.s. not significant, *p < 0.1, **p < 0.01, ***p < 0.001, ****p < 0.0001.

CEDT, whereby PFC facilitates electron transfer *via* liquid–liquid CEC, catalyzing the reduction of endogenous H_2O_2 to generate $^{\bullet}OH$ that induces tumor cell death.

The activation of ROS-mediated immune response *in vivo* was further confirmed. As shown in Fig. 9a, immunofluorescence staining for tumor-associated macrophages ($CD11b^+$) in tumor tissues revealed that, following treatment, the ROS generated induced ICD of tumor cells, with the released tumor-associated antigens attracting macrophages to accumulate at the tumor site.[11] Notably, the number of macrophages in the tumor region of mice in the PFC + GOD + US group increased 3.6-fold compared to the Control group, accompanied by a shift

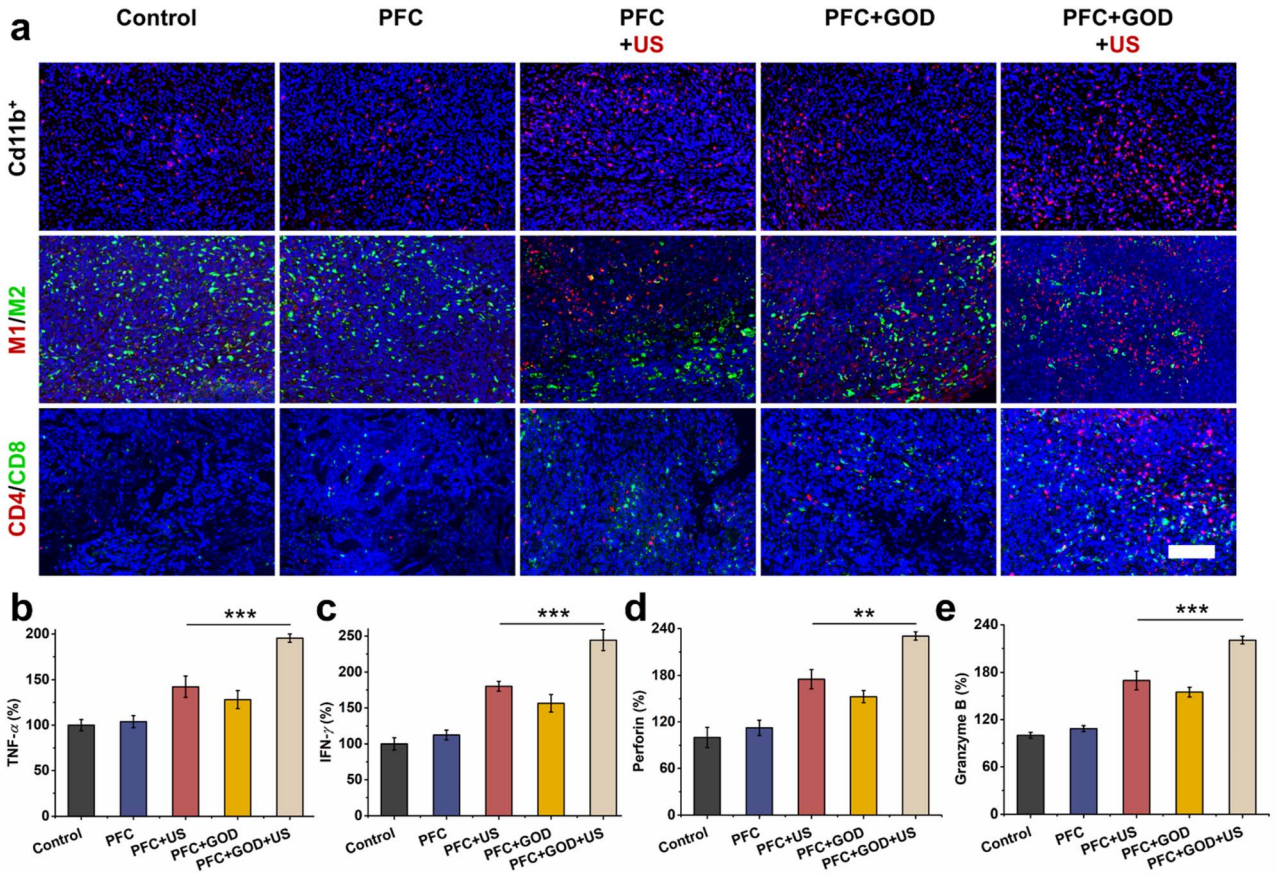

Fig. 9 (a) Representative immunofluorescence images of the distribution of $CD11b^+$, M1/M2, and $CD4^+/CD8^+$ T cells in the tumor tissues of different groups. Scale bar: 100 μm. Percentage of cytokine (b) TNF-α, (c) IFN-γ, (d) perforin, and (e) granzyme B content from tumors. n.s. not significant, *$p < 0.1$, **$p < 0.01$, ***$p < 0.001$, ****$p < 0.0001$.

from M2-type to M1-type macrophages. Specifically, in the PFC + GOD + US group, the quantity of M1 tumor-associated macrophages (TAMs) was 2.5 times higher than that of the Control group, while the number of M2-TAMs was 4.3 times lower. This reversal successfully transformed a "cold" tumor microenvironment into a "hot" one, thereby facilitating the presentation of tumor-associated antigens to T cells.[39] In stark contrast to the Control group, the PFC + GOD + US group exhibited a marked accumulation of T cells at the tumor site, promoting their differentiation into cytotoxic $CD4^+/CD8^+$ T cells. Moreover, these activated T cells secrete TNF-α, IFN-γ, granzyme, and perforin to kill cancer cells (Fig. 9b–e), activate apoptotic signaling pathways, and trigger an adaptive immune response to combat the tumor.[11,39]

Conclusion

In conclusion, this study introduces a novel mechanism by which the PFC–water liquid–liquid contact electrification (CE) spontaneously catalyzes the conversion of H_2O_2 into $^{\bullet}OH$, offering a more efficient alternative CEC reduction pathway that replaces the conventional ORR route. We demonstrated that PFC nanoemulsions can effectively catalyze $^{\bullet}OH$ production from H_2O_2 without the need for ultrasound, whereas the traditional ORR pathway requires ultrasonic energy to overcome the reaction energy barrier. Detailed ESR and mass spectrometry analyses revealed that PFC nanoemulsions act as electron-transfer mediators: electrons are initially captured from OH^- and subsequently transferred to H_2O_2 to produce $^{\bullet}OH$. Moreover, ultrasound treatment significantly enhances $^{\bullet}OH$ generation by increasing the frequency of liquid–liquid contact and providing additional energy *via* phonon excitation, thereby assisting the electron release from negatively charged PFC* back to H_2O_2. Importantly, this work demonstrates that the ROS generation pathway in CEDT is not solely dependent on the previously reported WOR and ORR CEC mechanisms but also involves an alternative CEC mechanism based on an H_2O_2 reduction pathway. This represents the hidden mechanism underlying CEDT, wherein PFC facilitates electron transfer through liquid–liquid CE, catalyzing the reduction of endogenous H_2O_2 to generate $^{\bullet}OH$ that ultimately induces tumor cell death.

Overall, our findings show that chemically inert PFCs can exhibit catalytic activity through liquid–liquid CE, with the generated ROS effectively mediating tumor cell apoptosis. These results underscore the catalytic potential of PFCs, further the development of CEDT, and provide a foundational understanding for novel catalytic strategies driven by interfacial CE.

Methods

Preparation of PFC nanoemulsions

First, HSA (16 mg) was dissolved in H_2O (8 mL) and stirred for 4 h to form an HSA solution (2 mg mL^{-1}). The HSA solution (2 mg mL^{-1}, 8 mL) was then mixed with PFTBA (300 μL) and stirred for 20 min and used with a cell crusher (SCIENTZ-II. D, China) and the mixed solution was sonicated for 20 min to form a PFC nanoemulsion. Then, the PFC nanoemulsion solution was collected by ultrafiltration centrifugation (8000 rpm, 10 min).

Detection of ROS by ESR

A PFC nanoemulsion (0.2 mg mL^{-1}) was prepared in DMPO (10 mM) solution with or without H_2O_2 (100 mM). The solution was then vortexed for 10 min. The ESR spectra of the mixed solution were obtained by electron paramagnetic resonance (EPR) spectrometry (Bruker magnettech ESR5000, Germany). To detect ROS by DMPO at different vortex times (0, 5, 10, 20 min), H_2O_2 concentrations (0, 20, 100, 200 mM), PFC nanoemulsion concentrations (0, 0.005, 0.2, 0.4 mg mL^{-1}), experiments were performed using the same procedure as above.

Intracellular H_2O_2 detection assay

4T1 cells (8×10^4) were seeded in 6-well plates and cultured for 12 h. Cells were then incubated with PFC NEs (30 μg mL^{-1}), GOD (0.2 μg mL^{-1}), and PFC NEs (30 μg mL^{-1}) combined with GOD (0.2 μg mL^{-1}) for 2 hours, with or without sonication (30 kHz, 2.0 W cm^{-2}, 5 min). The concentration of hydrogen peroxide in the cells was monitored by the hydrogen peroxide assay kit according to the protocol provided.

Monitoring of intracellular ROS production

DCFH-DA was used as a fluorescent indicator to monitor intracellular ROS production. 4T1 cells (8×10^3) were seeded in special Petri dishes and incubated for 12 h at 37 °C in a 5% CO_2 atmosphere. Next, cells were incubated with PFC NEs (30 μg mL^{-1}), GOD (0.2 μg mL^{-1}), and PFC NEs (30 μg mL^{-1}) combined with GOD (0.2 μg mL^{-1}) for 4 h, washed with PBS, and then stained with DCFH-DA (10 μM) for 15 min. They were then treated with or without sonication (30 kHz, 2.0 W cm^{-2}) for 10 min and then incubated at 37 °C for 2 h at 5% CO_2. After that, the medium was removed and the cell fluorescence was characterized by confocal laser scanning microscopy (TCS SP5, Leica, Germany).

Animal experimentation

The detailed animal experimental procedures are provided in the SI. All animal procedures were performed in accordance with the Guidelines for Care and Use of Laboratory Animals of Wuhan University and approved by the Animal Ethics Committee of Wuhan University.

Author contributions

Haimei Li: data curation, project administration, validation, writing – original draft, experimental design. Airong Xie: data curation, project administration, validation. Chengzi Hong: project administration, experimental design. Zicheng Wang: software, supervision. Zhong Lin Wang: project administration, methodology, investigation. Yi Liu: project administration, funding acquisition. Peng Jiang: project administration, funding acquisition, writing – review & editing. All the authors have approved the final manuscript.

Conflicts of interest

The authors declare no competing financial interest.

Data availability

The data supporting this article have been included as part of the supplementary information (SI). Supplementary information: experimental procedures, TEM image, ESR spectra, absorption spectra and fluorescence spectrum. See DOI: **https://doi.org/10.1039/d5sc05862g**.

Acknowledgements

This research was supported by the National Natural Science Foundation of China (U23A2089, 22403070), the National Postdoctoral Program for Innovative Talents (BX20230268), the China Postdoctoral Science Foundation (2023M742690), the Natural Science Foundation of Hubei Province (2025AFA009), Beijing Key Laboratory of High-Entropy Energy materials and Devices (Beijing Institute of Nanoenergy and Nanosystems) (No. GS2025ZD007, No. GS2025MS019), and the Large-scale Instrument and Equipment Sharing Foundation of Wuhan University.

References

1 J. Nie, Z. Ren, L. Xu, S. Lin, F. Zhan, X. Chen and Z. L. Wang, Probing contact-electrification-induced electronand ion transfers at a liquid-solid interface, *Adv. Mater.*, 2020, **32**, e1905696.
2 S. Lin, X. Chen and Z. L. Wang, Contact electrification at the liquid-solid interface, *Chem. Rev.*, 2022, **122**, 5209–5232.
3 Z. L. Wang and A. C. Wang, On the origin of contact-electrification, *Mater. Today*, 2019, **30**, 34–51.
4 Z. Wang, A. Berbille, Y. Feng, S. Li, L. Zhu, W. Tang and Z. L. Wang, Contact-electro-catalysis for the degradation of organic pollutants using pristine dielectric powders, *Nat. Commun.*, 2022, **13**, 130.
5 Z. Wang, X. Dong, W. Tang and Z. L. Wang, Contact-electrocatalysis (CEC), *Chem. Soc. Rev.*, 2024, **53**, 4349.
6 M. Zhang, W.-Z. Song, T. Chen, D.-J. Sun, D.-S. Zhang, C.-L. Li, R. Li, J. Zhang, S. Ramakrishna and Y.-Z. Long, Rotation-mode liquid-solid triboelectric nanogenerator for efficient contact-electro-catalysis and adsorption, *Nano Energy*, 2023, **110**, 108329.
7 J. Zhao, X. Zhang, J. Xu, W. Tang, Z. L. Wang and F. R. Fan, Contact-electro-catalysis for direct synthesis of H_2O_2 under ambient conditions, *Angew. Chem., Int. Ed.*, 2023, **62**, e202300604.

8 H. Li, A. Berbille, X. Zhao, Z. Wang, W. Tang and Z. L. Wang, A contact-electro-catalytic cathode recycling method for spent lithium-ion batteries, *Nat. Energy*, 2023, **8**, 1137–1144.
9 M. P. Murphy, H. Bayir, V. Belousov, C. J. Chang, K. J. A. Davies, M. J. Davies, T. P. Dick, T. Finkel, H. J. Forman, Y. Janssen-Heininger, D. Gems, V. E. Kagan, B. Kalyanaraman, N.-G. Larsson, G. L. Milne, T. Nyström, H. E. Poulsen, R. Radi, H. Van Remmen, P. T. Schumacker, P. J. Thornalley, S. Toyokuni, C. C. Winterbourn, H. Yin and B. Halliwell, Guidelines for measuring reactive oxygen species and oxidative damage in cells and *in vivo*, *Nat. Metab.*, 2022, **4**, 651–662.
10 Y. Zhao, Y. Liu, Y. Wang, S. Li, Y. Liu, Z. L. Wang and P. Jiang, The process of free radical generation in contact electrification at solid-liquid interface, *Nano Energy*, 2023, **112**, 108464.
11 H. Li, Z. Wang, X. Chu, Y. Zhao, G. He, Y. Hu, Y. Liu, Z. L. Wang and P. Jiang, Free radicals generated in perfluorocarbon-water (liquid-liquid) interfacial contact electrification and their application in cancer therapy, *J. Am. Chem. Soc.*, 2024, **146**(17), 12087–12099.
12 X. Dong, Z. Wang, Y. Hou, Y. Feng, A. Berbille, H. Li, Z. L. Wang and W. Tang, Regulating contact-electro-catalysis using polymer/metal janus composite catalysts, *J. Am. Chem. Soc.*, 2024, **146**, 28110–28118.
13 H. Zou, Y. Zhang, L. Guo, P. Wang, X. He, G. Dai, H. Zheng, C. Chen, A. C. Wang, C. Xu and Z. L. Wang, Quantifying the triboelectric series, *Nat. Commun.*, 2019, **10**, 1427.
14 A. Berbille, X. F. Li, Y. Su, S. Li, X. Zhao, L. Zhu and Z. L. Wang, Mechanism for generating H_2O_2 at water-solid interface by contact-electrification, *Adv. Mater.*, 2023, 2304387.
15 Z. Hu, H. Tan, Y. Ye, W. Xu, J. Gao, L. Liu, L. Zhang, J. Jiang, H. Tian, F. Peng and Y. Tu, NIR-actuated ferroptosis nanomotor for enhanced tumor penetration and therapy, *Adv. Mater.*, 2024, **36**, 2412227.
16 S. Zhong, K. Hu, Y. Wang, Z. Zhu, H. Zhou, J. Chen, S. Ren, C. Zhou, P. Zhou, B. Lai, X. Duan and S. Wang, Hierarchically ordered porous carbon crystals for nanoconfined and sustainable fenton oxidation of water pollutants, *Appl. Catal. B Environ.*, 2025, **361**, 124665.
17 W. Li, J. Tu, J. Sun, Y. Zhang, J. Fang, M. Wang, X. Liu, Z. Q. Tian and F. Ru Fan, Boosting reactive oxygen species generation via contact-electro-catalysis with Fe^{III}-initiated self-cycled Fenton system, *Angew. Chem., Int. Ed.*, 2024, **64**(1), e202413246.
18 X. Jia, E. Wang and J. Wang, Rational design of nanozymes for engineered cascade catalytic cancer therapy, *Chem. Rev.*, 2025, **125**(5), 2908–2952.
19 H. Li, Y. Liu, S. Li, S. Zhang, B. Huang, R. Cui, Y. Liu and P. Jiang, Cu-Doped black phosphorus quantum dots as multifunctional Fenton nanocatalyst for boosting synergistically enhanced H_2O_2-guided and photothermal chemodynamic cancer therapy, *Nanoscale*, 2022, **14**(10), 3788–3800.
20 J. Yang, B. Ren, H. Cai, W. Xiong, J. Feng, Q. Fan, Z. Li, L. Huang, C. Yan, Y. Li, C. Chen and Z. Shen, Cyclic catalysis of intratumor $Fe^{3+/2+}$ initiated by a hollow mesoporous iron sesquioxide nanoparticle for ferroptosis therapy of large tumors, *Biomaterials*, 2025, **313**, 122793.
21 F. L. Gomes, S. H. Jeong, S. R. Shin, J. Leijten and P. Jonkheijm, Engineering synthetic erythrocytes as next-generation blood substitutes, *Adv. Funct. Mater.*, 2024, **34**(28), 2315879.
22 X. Song, L. Feng, C. Liang, K. Yang and Z. Liu, Ultrasound triggered tumor oxygenation with oxygen-shuttle nanoperfluorocarbon to overcome hypoxia-associated resistance in cancer therapies, *Nano Lett.*, 2016, **16**(10), 6145–6153.
23 K. von der Hardt, M. A. Kandler, G. Brenn, K. Scheuerer, E. Schoof, J. Dötsch and W. Rascher, Comparison of aerosol therapy with different perfluorocarbons in surfactant-depleted animals, *Crit. Care Med.*, 2004, **32**(5), 1200–1206.
24 N. Kakaei, R. Amirian, M. Azadi, G. Mohammadi and Z. Izadi, Perfluorocarbons: A perspective of theranostic applications and challenges, *Front. Bioeng. Biotechnol.*, 2023, **11**, 1115254.
25 W. Wang, Y. Cheng, P. Yu, H. Wang, Y. Zhang, H. Xu, Q. Ye, A. Yuan, Y. Hu and J. Wu, Perfluorocarbon regulates the intratumoural environment to enhance hypoxia-based agent efficacy, *Nat. Commun.*, 2019, **10**(1), 1580.
26 H. Li, Y. Liu, B. Huang, C. Zhang, Z. Wang, W. She, Y. Liu and P. Jiang, Highly efficient gsh-responsive "off-on" NIR-II fluorescent fenton nanocatalyst for multimodal imaging-guided photothermal/chemodynamic synergistic cancer therapy, *Anal. Chem.*, 2022, **94**(29), 10470–10478.
27 C. J. Chen and E. Williams, Are hydroxyl radicals spontaneously generated in unactivated water droplets?, *Angew. Chem., Int. Ed.*, 2024, e202407433.
28 S. Bose, M. Mofidfar and R. N. Zare, Direct conversion of N_2 and air to nitric acid in gas-water microbubbles, *J. Am. Chem. Soc.*, 2024, **146**(40), 27964–27971.
29 X. Song, C. Basheer, Y. Xia and R. N. Zare, Oxidation of ammonia in water microdroplets produces nitrate and molecular hydrogen, *Environ. Sci. Technol.*, 2024, **58**(36), 16196–16203.
30 X. Song, C. Basheer and R. N. Zare, Water microdroplets-initiated methane oxidation, *J. Am. Chem. Soc.*, 2023, **145**(50), 27198–27204.
31 C. Dong, X. Dai, X. Wang, Q. Lu, L. Chen, X. Song, L. Ding, H. Huang, W. Feng, Y. Chen and M. Chang, A calcium fluoride nanozyme for ultrasound-amplified and Ca^{2+}-overload-enhanced catalytic tumor nanotherapy, *Adv. Mater.*, 2022, **34**(43), 2205680.
32 A. Berbille, X. F. Li, Y. Su, S. Li, X. Zhao, L. Zhu and Z. L. Wang, Mechanism for generating H_2O_2 at water-solid interface by contact-electrification, *Adv. Mater.*, 2023, e2304387.
33 L. Cao, C. Yang, B. Zhang, K. Lv, M. Li and K. Deng, Synergistic photocatalytic performance of cobalt tetra(2-hydroxymethyl-1,4-dithiin)porphyrazine loaded on zinc oxide nanoparticles, *J. Hazard. Mater.*, 2018, **359**, 388–395.

34 S. Cong, J. Cai, X. Li, J. You, L. Wang and X. Wang, Direct z-scheme xylan-based carbon dots@TiO_{2-x} nanocomposites for visible light driven photocatalytic of dye degradation and antibacterial, *Adv. Funct. Mater.*, 2024, **34**(32), 2401540.
35 C. Wu, L. Zhu, Q. Lu, H. Li, Y. Zhang and S. Yao, A dual-signal colorimetric and ratiometric fluorescent nanoprobe for enzymatic determination of uric acid by using silicon nanoparticles, *Microchim. Acta*, 2019, **186**(12), 754.
36 M. Angelaki, Y. Carreira Mendes Da Silva, S. Perrier and C. George, Quantification and mechanistic investigation of the spontaneous H_2O_2 generation at the interfaces of salt-containing aqueous droplets, *J. Am. Chem. Soc.*, 2024, **146**(12), 8327–8334.
37 Z. H. Loh, G. Doumy, C. Arnold, L. Kjellsson, S. H. Southworth, A. Al Haddad, Y. Kumagai, M. F. Tu, P. J. Ho, A. M. March, R. D. Schaller, M. S. B. Yusof, T. Debnath, M. Simon, R. Welsch, L. Inhester, K. Khalili, K. Nanda, A. I. Krylov, S. Moeller, G. Coslovich, J. Koralek, M. P. Minitti, W. F. Schlotter, J. E. Rubensson, R. Santra and L. Young, Observation of the fastest chemical processes in the radiolysis of water, *Science*, 2020, **367**(6474), 179–182.
38 T. Gan, Z. Yang, S. Li, H. Qian, Z. Li, J. Liu, P. Peng, J. Bai, H. Liu, Z. Wang and D. Wei, Unveiling janus chemical processes in contact-electro-chemistry through oxygen reduction reactions, *J. Am. Chem. Soc.*, 2025, **147**(29), 25407–25416.
39 H. Li, X. Yang, Z. Wang, W. She, Y. Liu, L. Huang and P. Jiang, A near-infrared-II fluorescent nanocatalyst for enhanced CAR T cell therapy against solid tumor by immune reprogramming, *ACS Nano*, 2023, **17**(12), 11749–11763.